



Cite this: *Mater. Horiz.*, 2021, 8, 3334

Received 12th June 2021,  
Accepted 15th September 2021

DOI: 10.1039/d1mh00925g

rsc.li/materials-horizons

## Freeform direct laser writing of versatile topological 3D scaffolds enabled by intrinsic support hydrogel<sup>†</sup>

Sebastian Hasselmann, <sup>a</sup> Lukas Hahn, <sup>b</sup> Thomas Lorson, <sup>b</sup> Eva Schätzlein, <sup>c</sup> Isabelle Sébastien, <sup>d</sup> Matthias Beudert, <sup>e</sup> Tessa Lühmann, <sup>e</sup> Julia C. Neubauer, <sup>d</sup> Gerhard Sextl, <sup>f</sup> Robert Luxenhofer <sup>\*bg</sup> and Doris Heinrich <sup>fhi</sup>

**In this study, a novel approach to create arbitrarily shaped 3D hydrogel objects is presented, wherein freeform two-photon polymerization (2PP) is enabled by the combination of a photosensitive hydrogel and an intrinsic support matrix. This way, topologies without physical contact such as a highly porous 3D network of concatenated rings were realized, which are impossible to manufacture with most current 3D printing technologies. Micro-Raman and nanoindentation measurements show the possibility to control water uptake and hence tailor the Young's modulus of the structures via the light dosage, proving the versatility of the concept regarding many scaffold characteristics that makes it well suited for cell specific cell culture as demonstrated by cultivation of human induced pluripotent stem cell derived cardiomyocytes.**

### New concepts

This contribution describes how a significant limitation of freeform direct laser writing of low viscosity resins can be overcome to fabricate complex topological 3D structures. When attempting to manufacture very small feature sizes of soft photocurable materials such as hydrogels, the residual mobility of the microstructures from convection or diffusion can prevent a high accuracy and precision, in particular when attempting to connect structures printed at different time points inside a liquid precursor. To overcome this issue, we introduce a thermo-responsive support gel that can be conveniently mixed with the resin at low temperature (5–10 °C) but forms a highly transparent solid gel at room temperature and above. This drastic increase in viscosity of the gel effectively suppresses diffusion and convection, keeping any freeform laser written soft structure securely in place during processing. After 3D freeform structuring is completed, the hydrogel can be easily removed by washing with water, developing intricate soft microstructures such as arrays of 3D concatenated hydrogel rings demonstrated in this contribution. This very simple approach opens new avenues to create soft microstructures at very high resolution, which are otherwise difficult to realize.

<sup>a</sup> Fraunhofer Project Center for Stem Cell Process Engineering Neunerplatz 2, Würzburg 97082, Germany

<sup>b</sup> Functional Polymer Materials, Chair for Advanced Materials Synthesis, Institute for Functional Materials and Biofabrication, Department of Chemistry and Pharmacy, University of Würzburg, Röntgenring 11, 97070, Germany

<sup>c</sup> East Bavarian Technical University of Applied Sciences, Prüfeninger Str. 58, Regensburg 93049, Germany

<sup>d</sup> Fraunhofer Institute for Biomedical Engineering, Fraunhofer Project Center for Stem Cell Process Engineering, Neunerplatz 2, Würzburg 97082, Germany

<sup>e</sup> Institute of Pharmacy and Food Chemistry, University of Würzburg, Am Hubland, Würzburg 97074, Germany

<sup>f</sup> Fraunhofer Institute for Silicate Research ISC, Neunerplatz 2, Würzburg 97082, Germany. E-mail: Doris.Heinrich@isc.fraunhofer.de

<sup>g</sup> Soft Matter Chemistry, Department of Chemistry and Helsinki Institute of Sustainability Science, Faculty of Science University of Helsinki, Helsinki 00014, Finland. E-mail: robert.luxenhofer@helsinki.fi

<sup>h</sup> Institute for Bioprocessing and Analytical Measurement Techniques, Rosenhof, Heilbad Heiligenstadt 37308, Germany

<sup>i</sup> Faculty for Mathematics and Natural Sciences, Ilmenau University of Technology, Ilmenau, Germany

<sup>†</sup> Electronic supplementary information (ESI) available. See DOI: 10.1039/d1mh00925g

A major objective of all biofabrication technologies is to combine a high three-dimensional printing resolution on the order of subcellular (<10 µm) or macromolecular (~100 nm) features with high processing speed to create complex and large sized tissue.

To mimic the physiological 3D environment of living cells, many aspects of material properties have to be considered and adapted, since the native extracellular matrix (ECM) is a highly complex, dynamic and heterogeneous environment,<sup>1,2</sup> which is essential for cell and tissue development. Its biophysicochemical interactions with the cells' membrane trigger diverse inter- and intracellular responses<sup>3</sup> leading to signal cascades, which regulate cell functions like adhesion, proliferation, differentiation and gene expression.<sup>4–6</sup>

One basic approach in the field of biofabrication is to mimic the native environment and seed viable cells onto a 3D scaffold that provides adhesion sites for further cell cultivation and



tissue maturation. In the natural ECM, this is enabled by the loosely intertwined, yet mechanically strong, densely packed extracellular matrix proteins. Since cells are capable of sensing this environment with submicron resolution,<sup>7</sup> and are highly influenced by the 2D and 3D morphology of the substrate,<sup>8,9</sup> a scaffold fabrication technique with corresponding submicron resolution is needed. Several rapid prototyping methods were established within recent years for the generation of 3D scaffolds for cell support. These range from electrospinning<sup>10</sup> and nozzle-based extruding systems<sup>11</sup> to inkjet printing<sup>12</sup> and light curing methods,<sup>13</sup> each with different accessible domains regarding the processed material, processing time, costs and resolution.<sup>14–16</sup>

Specialized cells such as fibroblasts, particular cells of the immune system, and tumor cells can migrate through the shiftable mesh of collagen fibers inside the ECM.<sup>17–19</sup> Using conventional 3D printing setups, mimicking such concatenated elements in an artificial 3D scaffold, requires support structures to suppress dislocation of loosely interconnected parts during the production. For solid or highly viscous precursor materials, such as ORMOCER®'s the resin itself can lend support as the structures are embedded in the rigid matrix and *e.g.* concatenated rings have been successfully demonstrated with the photoresist SZ2080.<sup>20</sup> However, for low viscosity resins, diffusion results in an immediate position loss of polymerized parts, making fabrication of complex or intertwined structures a particular challenge. Accordingly, freely movable yet concatenated components have not been realized with cell-friendly soft materials such as hydrogels to date. However, such materials are essential to model biological tissue.<sup>21–23</sup>

Within additive manufacturing, the direct laser writing technology based on two-photon polymerization (2PP) offers the highest lateral resolution reaching values below 100 nm.<sup>24,25</sup> At the same time, 2PP is applicable to a broad selection of material classes, *e.g.* hydrogels,<sup>26–28</sup> diverse polymers,<sup>29,30</sup> or multifunctional composites.<sup>31</sup> Along with the 3D architectural freedom and the possibility of tailoring different material properties like crosslinking density or Young's modulus by optimizing the processing parameters,<sup>32</sup> make the 2PP a perfect candidate for the complex design of cellular scaffolds with sub-micron sized structural elements.

Most conventional 3D printing techniques working with the standard layer-by-layer method, lack two important features: first, they need a physical connections between all printed elements or use of support structures to stabilize delicate parts and overhangs, which have to be removed after the printing process. Consequently, entangled or concatenated elements are not possible especially when using soft materials like hydrogels. The second limitation of most conventional 3D printing setups is that they are not printing truly three-dimensional, since a CAD model undergoes the hatching–slicing procedure, resulting in an axial stacking of 2D layers (Fig. 1A). This limits the possible motion paths, for instance, a helical XYZ trajectory is not realizable without support structures. Furthermore, a large portion of the bounding box of the 3D model has to be scanned to build up the structure, although nothing is printed inside a

huge fraction of this volume. Since production time increases with the third power of increasing printing resolution, large sized samples produced with submicrometer resolution cannot be realized cost-effectively. With regard to 2PP, several approaches are utilized in order to overcome this problem using galvo-scanner setups, parallelization or beam shaping.<sup>33–35</sup> Easier and more common is the use of objectives with lower numerical aperture yielding a higher polymerized volume per time, albeit sacrificing resolution.<sup>36</sup>

Here, we present a novel approach that overcomes both limitations and is capable of creating truly 3D structural parts that are only topologically interconnected. We demonstrate that even delicate features down to 1 μm, made of a soft hydrogel are realizable and applicable as 3D cell scaffold. In contrast to the time-consuming layer-by-layer procedure, freeform 3D printing allows the construction of arbitrary shapes by moving along any XYZ trajectory without the creation of any support structures (Fig. 1B). Apart from the 2PP process<sup>37</sup> only few 3D printing technologies are capable of this true 3D freeform printing from metals<sup>38</sup> to hydrogels,<sup>39</sup> but are often limited regarding material selection and in particular, resolution.<sup>40</sup> In case of 2PP, the non-polymerized resin surrounds the structured parts during the production process, which instantaneously provides a 3D support (Fig. 1C). For low-viscosity materials like hydrogels however, the creation of an object such as a single ring, by moving the objective focus in a circular motion, would be impossible since the beginning of the ring moves from its initial position due to diffusion and gravity, preventing the completion of the structure (Fig. 1D, open joints of single rings are highlighted with arrows).

To extend the versatile and fast freeform 3D printing procedure to soft hydrogels of low-viscous precursors, we developed a two-component hydrogel composition (Fig. 1E) that results in a photocurable resin when mixed with a photoinitiator. Poly(ethylene glycol) diacrylate (PEG-DA,  $m_w = 700 \text{ g mol}^{-1}$ ) and Rose Bengal (RB) were chosen as photosensitive components and photoinitiator, respectively. RB has gained interest in the field of biomedical applications due to its versatile properties like antimicrobial activity and its use in photochemical tissue bonding and cancer therapy.<sup>41</sup> The second hydrogel component is a highly cytocompatible poly(2-oxazoline)/poly(2-oxazine) block copolymer (PMeOx-*b*-PnPrOzi, short: POx-*b*-POzi),<sup>42,43</sup> that undergoes a reversible sol–gel transition to a viscoelastic solid-like structure with increasing temperature (thermogelling).<sup>44,45</sup> In the cold, it is liquid and is readily mixed with the other components. As a gel at room temperature, it allows creation of freestanding elements without the need for support structures. Important to note, the POx-*b*-POzi support gel is only physically crosslinked and is readily washed away together with uncured PEG-DA (sol fraction) after the freeform 3D printing process (Fig. 1F) leading to the desired 3D structure (Fig. 1G). Due to the fragility of the structures, they were fabricated inside an ibidi chamber, which allowed for easy handling as well as long-term storage filled with liquid. Surrounded by water the hydrogel structures rise upwards due to buoyancy and do not require any additional support structures.

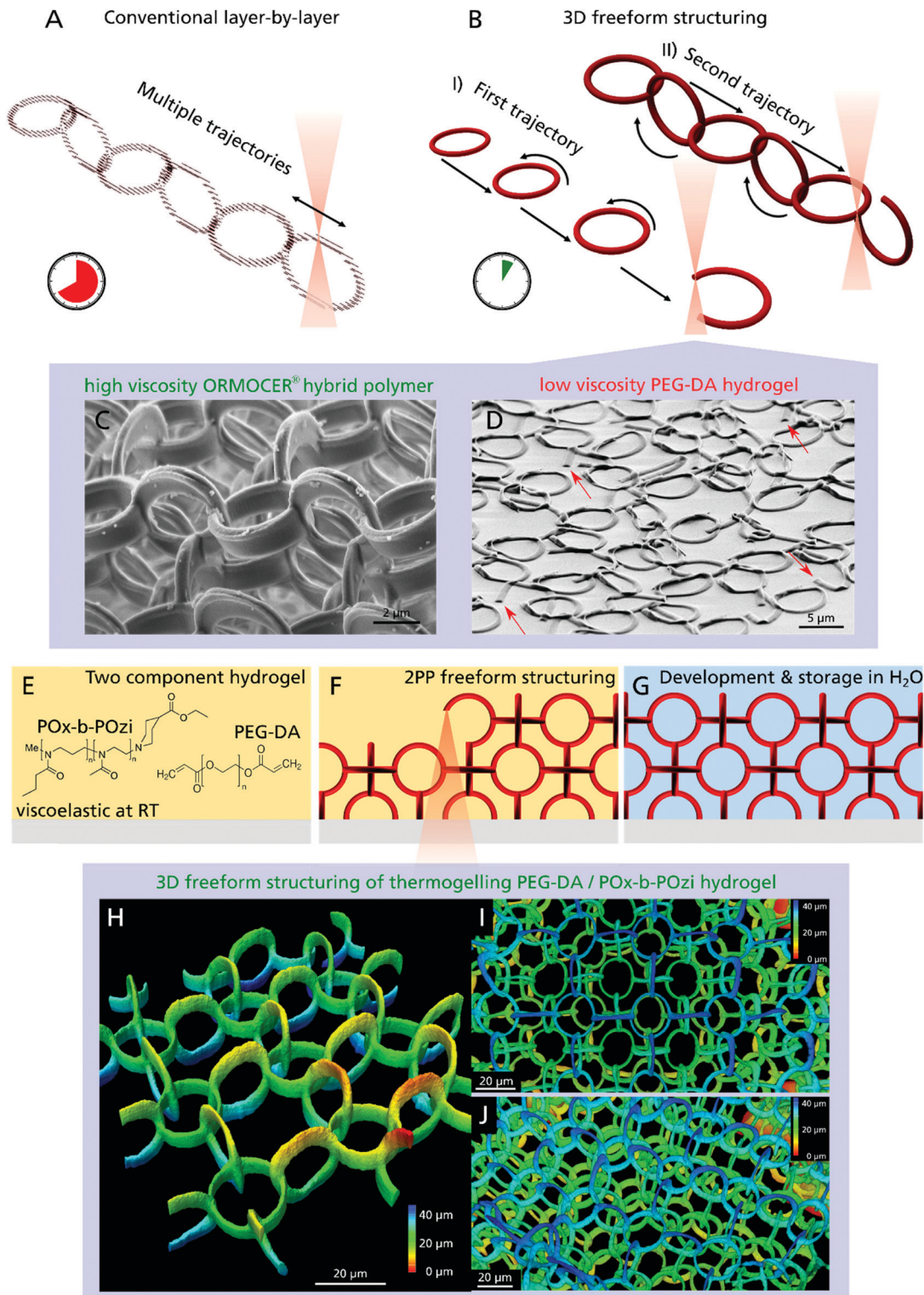


**Fig. 1** (A) Schematic hatching and slicing assembly of a 3D structure using the time consuming layer-by-layer procedure. (B) Trajectory of a laser focus during three-dimensional freeform structuring, which is applicable with high viscosity polymers that suppress diffusion of printed elements (C) but leads to discontinuous parts when structuring in low viscosity materials (D), open joints of single rings are highlighted by arrows. (E–G) Components and polymerization process of the two-component hydrogel, via freeform 2PP, followed by a development step dissolving all non-illuminated parts of the hydrogel including the intrinsic support matrix. (H) Confocal fluorescent microscopy image of interconnected rings with a diameter of 15  $\mu m$ . (I) Top-view and (J) side-view of an identical ring structure with three layers.

Investigations confirmed that freeform 2PP structuring is possible, demonstrated by a 3D chain mail like scaffold model, which is

composed of rings oriented in the XZ, YZ and XY plane (Fig. 1H: one layer, 1I: three layer (top view) and 1J three layer (side view)).



All rings of the same orientation are structured sequentially and although they are not connected to other polymerized parts they are stuck in place due to the intrinsic support hydrogel (Fig. 1B-I) and only become connected when structuring the second and third ring plane (Fig. 1B-II).

For this strategy to become feasible, the combination of photopolymerizable macromonomer and thermogel is critical by adjusting the rheological properties. While  $\text{POx-}b\text{-POzi}$  (storage modulus = 2.2 kPa) and the  $\text{POx-}b\text{-POzi/PEG-DA}$  mixture (storage modulus = 1.4 kPa) form solid gels at room temperature (Fig. 2A, 2B1 and 2), the PEG-DA solution (45 wt% in water) presents as a low viscosity liquid (storage modulus of 3 Pa at 1% strain) (Fig. 2A and B3), unable to suppress diffusion of polymerized structures inside the gel.

The hydrogel's mechanical properties will be an essential parameter for cell behavior<sup>21</sup> that can be tailored *via* the polymer crosslinking, which in turn can be controlled by the laser power and processing velocity. We used micro-Raman to investigate the curing behavior and polymer – water ratio depending on the 2PP process parameters (Fig. 2C). We analyzed all components of the investigated hydrogel composition separately, as well as the hydrogel mixture and cured/developed hydrogel cylinders (Fig. S1, ESI<sup>†</sup>). Overall, conversion of acrylate groups is high, as evidenced by the loss of acrylate signal in all investigated 2PP structures (Fig. 2C Inset). Notably, while the majority of the supporting hydrogel is dissolved during the development step, Raman spectra suggest that some  $\text{POx-}b\text{-POzi}$  remains in the printed structure even after washing (residual signals at  $2940\text{ cm}^{-1}$ ,  $1618\text{ cm}^{-1}$  and  $700\text{ cm}^{-1}$ ) (Fig. 2C, highlighted in grey). Whether  $\text{POx-}b\text{-POzi}$  chains are embedded covalently *via* chain transfer reactions or entangled in the PEG-DA network remains unclear at this point.

Focusing on the wavenumber range between  $2800\text{ cm}^{-1}$  and  $3600\text{ cm}^{-1}$ , and normalizing the spectra to the water band around  $3400\text{ cm}^{-1}$ , an increasing hydrogel signal (PEG-DA and  $\text{POx-}b\text{-POzi}$ ) between  $2800\text{ cm}^{-1}$  and  $3000\text{ cm}^{-1}$  correlates with increasing light dosage (exemplary for 33 mW and different velocities shown in Fig. 2D). This means that a higher 2PP light dosage yields a higher polymer – water fraction. In order to describe the ratio of polymer and water semi-quantitatively, we fitted the Raman bands to determine their area (example of Gaussian deconvolution of Raman peaks, see Fig. S2C, ESI<sup>†</sup>) for different combinations of laser power and velocity. The obtained polymer to water ratio (AP/AW) can be correlated with *e.g.* the processing velocity (Fig. 2E, blue data) or laser power (Fig. 2E, red data). After development, all 2PP structures exhibit lower AP/AW values compared to precursor mixture, confirming swelling during the development step. At constant laser power, the AP/AW drops rapidly with increasing processing speed from  $0.25\text{ mm s}^{-1}$  to  $1.5\text{ mm s}^{-1}$ , beyond which it remains stable above 0.2, which means that the velocity variation in that range does not change the final polymer properties significantly (Fig. 2E). However, for even higher velocity values, the degree of crosslinking will further decrease, resulting in incomplete parts of the written structures (Fig. S1, ESI<sup>†</sup>). At a constant velocity of  $0.25\text{ mm s}^{-1}$ , AP/AW remains constant for a laser power from

45 mW to 39 mW, indicating that the maximum interconnectivity for this material and setup is achieved. This is followed by an essentially linear decline with decreasing laser power. Since the laser power and processing velocity are tuned separately, they can be varied during the production, enabling adjustment of swelling/mechanical behavior on the fly with high spatial control to create mechanically anisotropic scaffolds by simply adjusting the 2PP process parameters.

Young's moduli of 2PP structured cylinders were measured by nanoindentation to correlate with the swelling degree (Fig. 2F). At 45 mW, the moduli increased from  $0.1\text{ MPa}$  to  $0.5\text{ MPa}$  with decreasing processing velocity (from  $2$  to  $0.25\text{ mm s}^{-1}$ ) exhibiting a similar trend as AP/AW, corroborating the direct correlation of processing parameters with physico-chemical properties of the material. In contrast to AP/AW values, the moduli level at  $0.5\text{ mm s}^{-1}$ , suggesting saturation of PEG-DA polymerization. Therefore, the higher AP/AW may be attributed to an increased retention of  $\text{POx-}b\text{-POzi}$ , which adds little influence on mechanical properties.

Due to their high water content hydrogels enable elastic modulus values of  $<1\text{ kPa}$  up to  $>1\text{ MPa}$ , depending on the material, crosslink density and molecular weight.<sup>46</sup> For PEG-DA with a molar mass of  $700\text{ g mol}^{-1}$  as used in this study, values from  $<100\text{ kPa}$  to around  $19\text{ MPa}$  are reported. The Young's modulus is strongly dependent on PEG-DA concentration and exposure conditions.<sup>47,48</sup>

To explore the potential of this novel material and approach, we designed 3D scaffold topologies, which are otherwise difficult to realize. Specifically, we compared concatenated and welded hydrogel rings. Identically oriented rings are structured along a straight line in a continuous motion, which alternates between circular phases at which the material is illuminated and the hydrogel polymerized, and linear phases without structuring (Fig. 1B). This yields smooth XYZ trajectories and allows high processing velocities with very small positioning errors, *e.g.* below  $0.5\text{ }\mu\text{m}$  at a velocity of  $0.5\text{ mm s}^{-1}$  and a ring diameter of  $20\text{ }\mu\text{m}$ . This deviations could only be observed for XZ and YZ oriented rings and depend strongly on the ring diameter and velocity (Tables S2 and S3, ESI<sup>†</sup>). When using a ring periodicity of exactly two times the ring diameter, the rings are welded together resulting in a freestanding 3D structure. When using smaller periodicities however, the polymerized volume of the rings do not overlap and the rings are not connected but are concatenated without initial physical contact. After developing, the hydrogel rings can move freely relative to each other, essentially forming a 3D chainmail structure. To produce multilayered samples, several ring layers are stacked upon each other with a shift of half a period in X and Y direction. A variety of ring-based structures have already been demonstrated,<sup>20,49</sup> but to the best of our knowledge, this is the first time that such highly concatenated microperiodic structure has been fabricated.

To determine in more detail the processing window for concatenated 3D ring structures an array of fields with four ring layers was produced, wherein laser power and structuring velocity were varied (Fig. 3A). Subsequently the structure quality was categorized using fluorescent confocal microscopy (Fig. 3B).



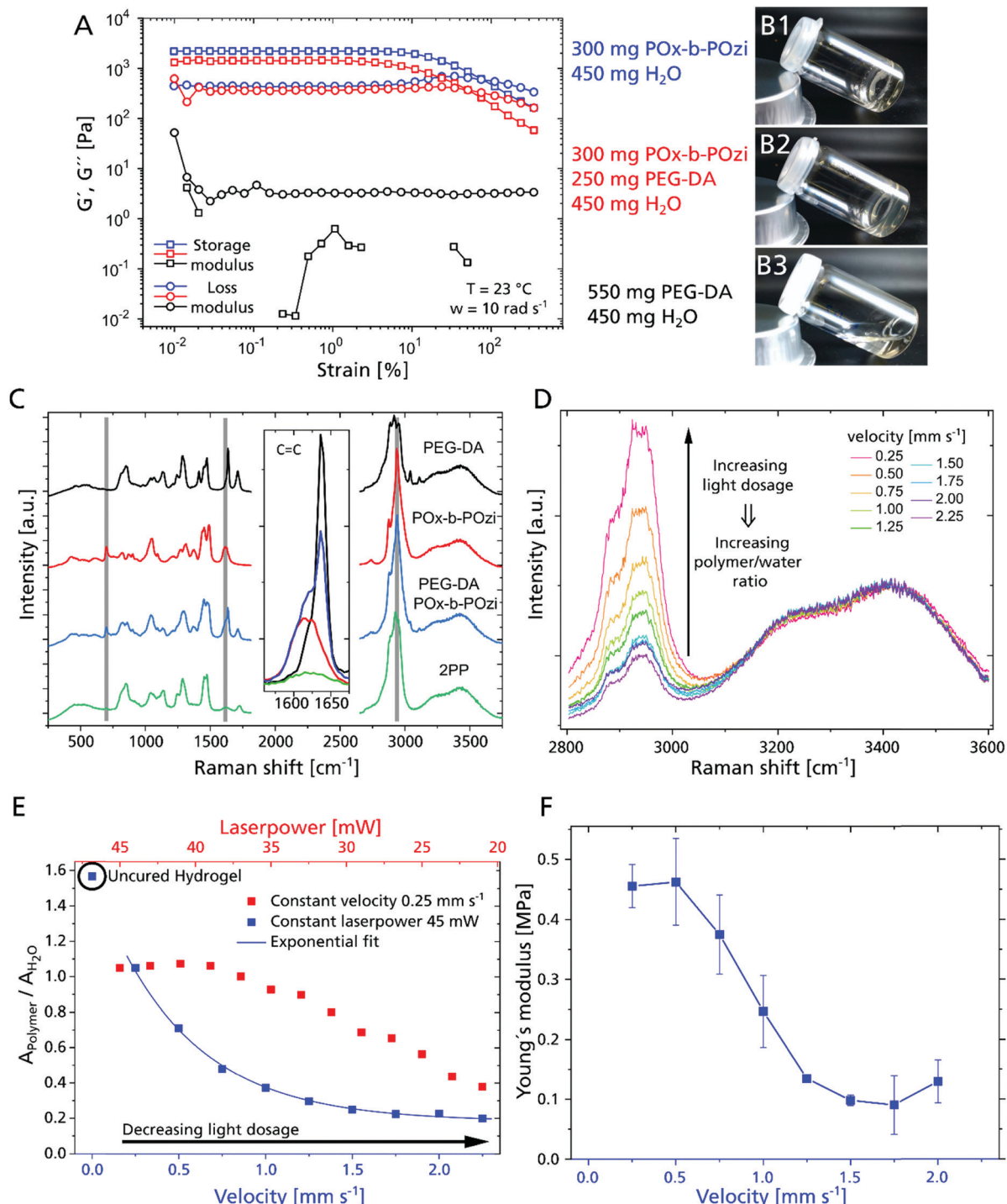


**Fig. 2** (A) Amplitude sweep of different hydrogel compositions: POx-*b*-POzi (B1), PEG-DA/POx-*b*-POzi mixture (B2) and PEG-DA (B3). (C) Comparison of Raman spectra of the main components PEG-DA and POx-*b*-POzi as well as the hydrogel mixture as prepared (PEG-DA/POx-*b*-POzi) and after 2PP structuring and development (2PP). (D) Raman spectra of 2PP structured cylinders with a constant laser power of 33 mW and increasing velocity from 0.25 mm s<sup>-1</sup> to 2.25 mm s<sup>-1</sup>. (E) Area ratio of fitted Raman bands of polymer and water depending on the structuring laser power (red) and velocity (blue). The value at 0 mm s<sup>-1</sup> corresponds to the unstructured PEG-DA/POx-*b*-POzi hydrogel. (F) Young's modulus of 2PP structured cylinders depending on the structuring velocity (error bars resulting from the standard error of the measurement).

We identified an optimized cluster of parameters with structuring velocities between 0.5–0.6 mm s<sup>-1</sup> at 46 mW and 0.1 mm s<sup>-1</sup> at 21 mW (Fig. 3A1 and B, green). For higher photon doses, the polymerized volume overlaps, resulting in

welded rings (Fig. 3A1 and B, blue), while incomplete and opened rings are formed when the dosage is insufficient (Fig. 3A4 and B, red). Between optimal and clearly inadequate conditions, sets of parameters are found, which yield

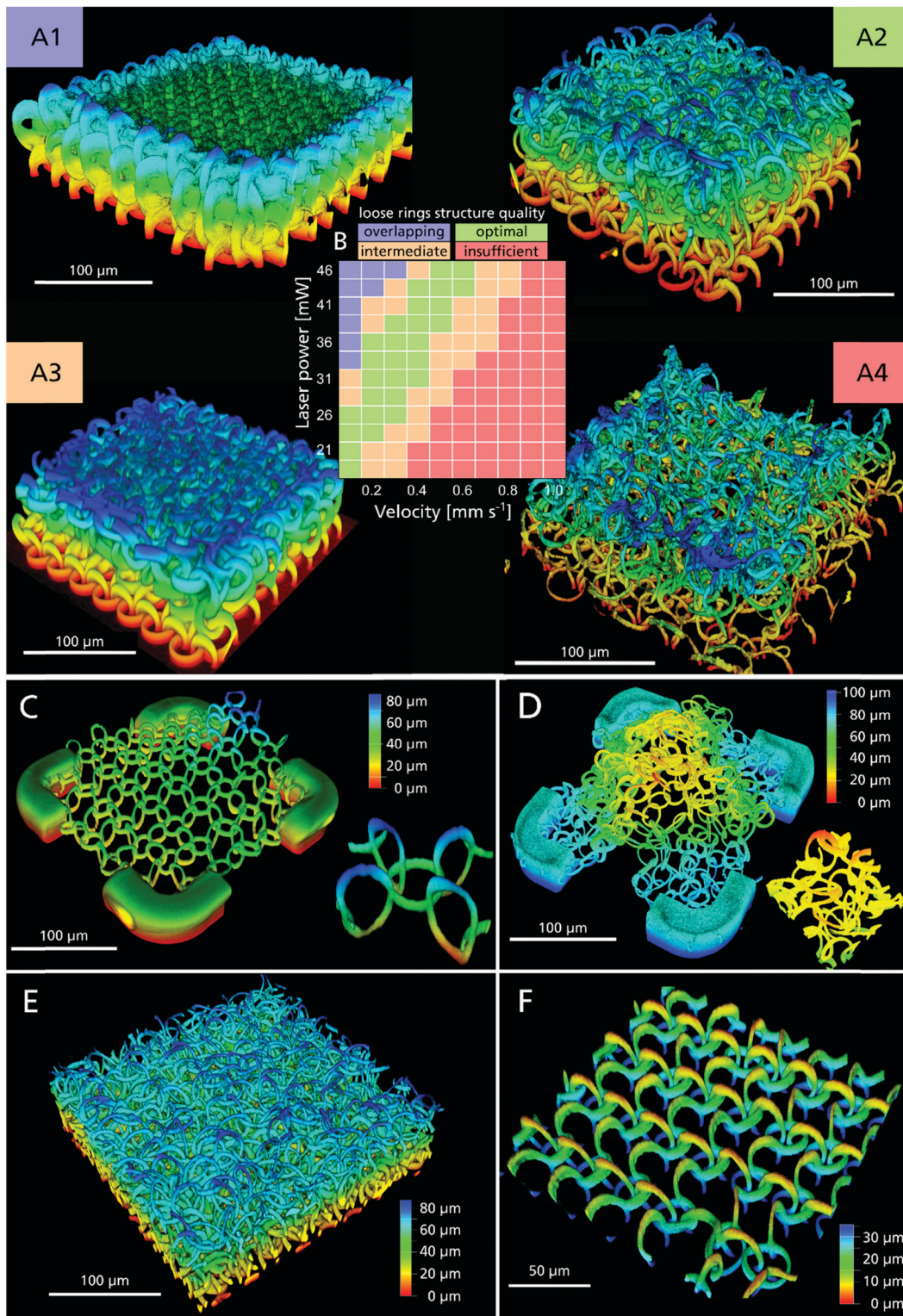


**Fig. 3** Confocal fluorescent microscopy images of different 2PP structured 3D designs. (A) Determination of 2PP processing window in order to achieve 3D loosely interconnected rings (concatenated ring configuration). (A1) Laser dosage too high, (A2) as desired, (A3) intermediate structure quality, (A4) laser dosage too low. (B) Matrix of investigated velocity and laser power combinations and their classification into the described categories. One layer of welded (C) and concatenated (D) rings free hanging inside a support structure. (E) A section of a 1 × 1 mm field made of four concatenated ring layers. (F) One layer of anisotropic interconnected rings (welded and concatenated ring configuration, depending on spatial direction).

inconsistent results (e.g. partially welded, partially concatenated rings) (Fig. 3A3 and B, orange).

To validate that these concatenated rings in the 3D scaffold are completely free to move in 3D, we connected one layer of

rings only by four lateral supporting edges to the substrate, *i.e.*, the rings were free-floating above the substrate and only surrounded by water. While the welded rings remain essentially in place and in the same height as they were structured (Fig. 3C and Video S1, ESI†), the concatenated rings moved relative to each other and rose in the medium due to buoyancy (Fig. 3D and Video S2, ESI†). When a flow of liquid is applied, it is possible to overcome the surface adhesion forces at the ring touching sites and the movement of the concatenated rings becomes clearly visible (ESI† Video S3). It must be stressed, that by the combination of concatenation and material properties, unique overall mechanical properties become available, much like a chainmail made of steel rings, which nevertheless is highly pliable.

Since the two-photon absorption is a non-linear optical effect, it is possible to create feature sizes below the Abbe diffraction limit. The point-spread-function (PSF) of the employed water objective with a numerical aperture of 1.2 has a theoretical FWHM of 0.30  $\mu\text{m}$  lateral and 0.82  $\mu\text{m}$  axial at a structuring wavelength of 705 nm.<sup>50</sup> With lower light dosages, smaller feature sizes are possible. This however also lowers its degree of polymerization and overall structure stability<sup>51</sup> (Fig. 3A1–A4). Therefore, the final 3D design has to be stable enough to endure externally applied forces during development, handling and sample preparation.

To estimate the smallest possible feature size, we measured the dimensions of one ring (shown in Fig. 3C), with the diameter increasing from 15  $\mu\text{m}$  by design to  $(17.7 \pm 0.3) \mu\text{m}$ , due to water uptake (Fig. S3, ESI†). Due to the spatial anisotropy of the PSF, the cross section of a single line is elliptical and amounts to  $(1.1 \pm 0.3) \mu\text{m}$  and  $(5 \pm 1) \mu\text{m}$  in the lateral and axial direction, respectively. Based on this, we can estimate the volume porosity for the scaffold design used for cell experiments with ring diameters of 20  $\mu\text{m}$  assuming a torus with a thickness of 2  $\mu\text{m}$ , which yields 98% porosity for the welded ring and 95% for the concatenated ring design. Fig. 3E shows a section of a 1 mm  $\times$  1 mm sized field, consisting of 16,428 rings, arranged in four layers and a ring diameter of 20  $\mu\text{m}$ . Although not optimized for speed, the fabrication of this comparably large yet high precision 3D scaffold took only 26 min and was only possible due to the utilization of the fast 3D freeform structuring method. Higher processing speeds can be achieved using higher laser dosage.

This design freedom enables heterogenic structures, for example by combining welded with loosely concatenated rings within one sample, for example in different directions (Fig. 3F and ESI† Video S4). Thus, anisotropic mechanical properties can be created and the structure behaves differently in fluid flow, applied from the *X* and the *Y* direction, respectively (see ESI† Video S5). This footage also reveals the flexibility of each individual ring resulting in a low overall Young's modulus. These designs might be useful to define preferential directions or anisotropic Young's moduli important for cardiac or neuronal cells growth, movement and maturation.

We performed force indentation measurements on four layers of concatenated rings. Obviously, the overall Young's

modulus is much lower compared to the bulk cylinder 2PP structures, since only a small volume fraction consists of crosslinked hydrogel, surrounded by liquid. Furthermore, indentation theorems like the Hertz model assume a homogeneous and isotropic material,<sup>52</sup> therefore the experimentally determined value of  $(0.14 \pm 0.11) \text{kPa}$  cannot be compared with the Young's modulus directly, and can only be used as very rough estimation. The high standard deviation of such measurements is caused by different contact areas depending on the measuring position and anisotropy of the structure. Nevertheless, all obtained values are far below 1 kPa, illustrating the material and structural flexibility of the 3D ring scaffold, making it a promising material for soft tissue cells, suitable even for neuronal cell cultivation.<sup>21</sup>

Compared to the numerous production methods that have been established in the field of biofabrication, the 2PP offers the highest 3D resolution. However, this also implies a low building rate, which is why the ratio of processed material per unit of time and the minimal feature size is used for better comparability. For the 2PP, this is  $0.05 \times 10^{-3} \text{ m}^2 \text{ min}^{-1}$ , while methods such as electrospinning and ink-jet reach values of  $0.1 \times 10^{-3} \text{ m}^2 \text{ min}^{-1}$  and stereolithography and bioplotting achieve  $0.5 \times 10^{-3} \text{ m}^2 \text{ min}^{-1}$ , respectively.<sup>24</sup> The high acquisition costs have certainly contributed to the fact that this technology has only hesitantly made its way into the industry. However, since several producers of 2PP systems have now established themselves on the market, it can be assumed that the price and the technological possibilities will continue to develop rapidly.

The requirements for optical properties and biocompatibility of photoresists and photoinitiators initially limited the materials that could be used for 2PP. However, many new materials have been developed in the field of photoinduced polymerization, which are also processable with 2PP, so that even composites<sup>53,54</sup> and multi-material samples<sup>55,56</sup> can be fabricated as is possible in bioplotting. In contrast to other light-based methods, 2PP does not require high-energy light, which is why polymerization in the presence of cells is also possible when using an infrared light source.<sup>57</sup> The significant main advantage, however, is the absolute freedom of design combined with very high resolution, especially the possibility of freeform structuring, which is impossible with most conventional 3D printing techniques. With our novel concept, it was possible to transfer this freedom of movement during structuring to low-viscosity materials in order to produce 3D formations that would otherwise be impossible or very challenging to realize, thus making novel 3D scaffold designs feasible in the future.

In order to investigate the use of the developed material as 3D scaffold, cellular interaction and behavior of L929 fibroblasts and human induced pluripotent stem cell (hiPSC) derived cardiomyocyte cells with various structures was investigated.

Cell adhesion on plain PEG hydrogels is known to be hindered due the non-fouling character of PEG, but can be improved by incorporating suitable adhesion molecules.<sup>22,23,58</sup> For this purpose, the hydrogel composition was supplemented with a RGD-motif (covalently attached *via* a maleimidohexanoic acid linker),



providing anchoring sites for integrins. An indirect indicator for the successful incorporation of the RGD-motif was the demand for increasing 2PP laser dosage with increasing RGD peptide concentration compared to the unmodified hydrogel composition (Fig. S4, ESI†), which can be attributed to the impact of the maleimide moiety on the polymerization. Maleimide has only one carbon double bond, which contributes to chain polymerization, whereas the diacrylate monomer unit of PEG has two. Therefore, the polymerization is statistically more likely to be terminated if the peptide is involved. Covalent integration of the RGD peptide into the polymer network was assessed by proliferation of GFP labeled L929 fibroblasts (Fig. 4A). The cells were cultured on a  $4 \times 4$  array of  $600 \mu\text{m}$  diameter 2D RGD-modified (ESI† Fig. S5A) or unmodified (ESI† Fig. S5B) hydrogel discs, respectively. One day after cell seeding, both samples were flipped upside down and cultivated overhead for six days (Fig. S5C (RGD-modified) and D (non-modified), ESI†). This ensured that only adherent cells were taken into account for proliferation, while non-adherent cells were discarded through medium exchange. Unexpectedly, cells were able to adhere to the PEG-DA sample also without RGD modification,<sup>59</sup> which might be promoted by the relatively high crosslinking or other incorporated components like POx-*b*-POzi and Rose Bengal.<sup>60</sup> With increasing incubation time however, the RGD-modified samples showed a higher number of adherent cells over time, which corroborates the incorporation of the RGD-motif and long-term effects on cell proliferation.

A 3D scaffold must provide mechanical stability to adherent cells and allow 3D cell migration. To investigate this, GFP-labelled L929 cells were seeded onto the 3D ring scaffolds and time-lapse images were acquired using confocal laser scanning microscopy. These demonstrate the advantage of Rose Bengal as photoinitiator, which acts as fluorophore inside the polymer, whose fluorescent signal can easily be separated from the green GFP channel. In both scaffold variations, the cells were able to penetrate the structure and move freely in all three dimensions (Fig. 4B: welded and C: concatenated). The ring diameter of  $20 \mu\text{m}$  offers a tradeoff between high structural porosity and mechanical support properties. The openings are small enough to prevent cells from falling through the scaffold onto the substrate during seeding, but are still large enough for cells to readily migrate through a single ring. Due to the different ring periodicity, the welded configuration features a 48% lower ring density in all dimensions and it exhibits linear channels without any obstacles for the cells throughout the 3D structure. For the concatenated design however, the rings are randomly distributed and a more confined cell motion was observed, but still cells can move freely by shifting the concatenated rings and open their path through the 3D scaffold. The more spherical cell morphology (Fig. 4B and C inset) is common for cells cultivated in a 3D environment and even more pronounced on soft surfaces.<sup>61</sup> The concatenated ring design with its movable elements is similar in structure to the ECM, where low viscosity compartments are pervaded by collagen fibres. These provide mechanical support to cells, but can also be moved and penetrated by them.<sup>1,19</sup> The flexibility of the complete 3D

structure is emphasized when occupied by many cells with the scaffold distorted or elongated in a specific direction (ESI† Video S6). In addition to the influence on the entire construct, single cells are able to bend and twist rings in their direct vicinity, corroborating the low Young's modulus of a single ring, as single cells are capable of exerting forces only in the pN–nN regime,<sup>62</sup> while cellular forces inside the human body reach orders of  $\mu\text{N}$ .<sup>63</sup> In the case of the welded rings, this distortion is elastic and the structure regains its original 3D configuration (ESI† Video S7). For the concatenated rings, this occurs as well, but often accompanied by a permanent change in the ring arrangement (ESI† Video S8) due to the lack of a reset force.

Due to the high versatility of presented approach in terms of material selection and adjustable properties along with the possibility to create geometrical (Fig. 3F) as well as mechanical (Fig. 2F) anisotropy, it is an exciting candidate for production of complex and cell type specific 3D scaffolds. For instance, a geometrical anisotropy can facilitate the microarchitecture and biological functions of cardiac cells<sup>64</sup> and support proliferation and maturation of cardiovascular tissue with high biological functionality, derived from hiPSC.<sup>65</sup> Mechanotransduction plays a vital role during their differentiation, maturation and tissue development in terms of cell alignment and cellular organization.

In preliminary tests, we seeded hiPSC-derived cardiomyocyte cell aggregates (Fig. 4D) and single cells (Fig. 4E) onto four-layered hydrogel ring scaffolds. They were cultivated for more than two weeks and spontaneous contractions were observed (ESI† Video S9). Cells interacted with the 3D substrate and its deformation is clearly visible, as well as the stretching of single rings (ESI† Video S10). At this stage cardiomyocyte cells are not fully matured and therefore do not exhibit a sarcomeric structure. Future studies will be conducted to adjust the scaffold design to thereby optimize the adhesion surface and improve cell maturation.

## Conclusions

We present an approach capable of producing topologically unusual cell scaffolds with a lateral feature size of  $1 \mu\text{m}$  based on two-photon polymerization (2PP) and overcoming the slow standard layer-by-layer procedure used in conventional 3D printing setups. This freeform printing approach decreases production time without sacrificing 3D resolution and offers freedom in design. Highly porous 3D scaffold designs are demonstrated based on welded, concatenated or 3D-interconnected rings with topological anisotropy, respectively. Such structures where previously inaccessible without complex support structures, especially for low viscosity precursors. We solved this problem by creating a two-component hydrogel: the first component is a photocurable hydrogel precursor, while the second is a thermoresponsive hydrogel providing a viscoelastic intrinsic support matrix for delicate microperiodic hydrogel structures. The crosslinking density and water content of



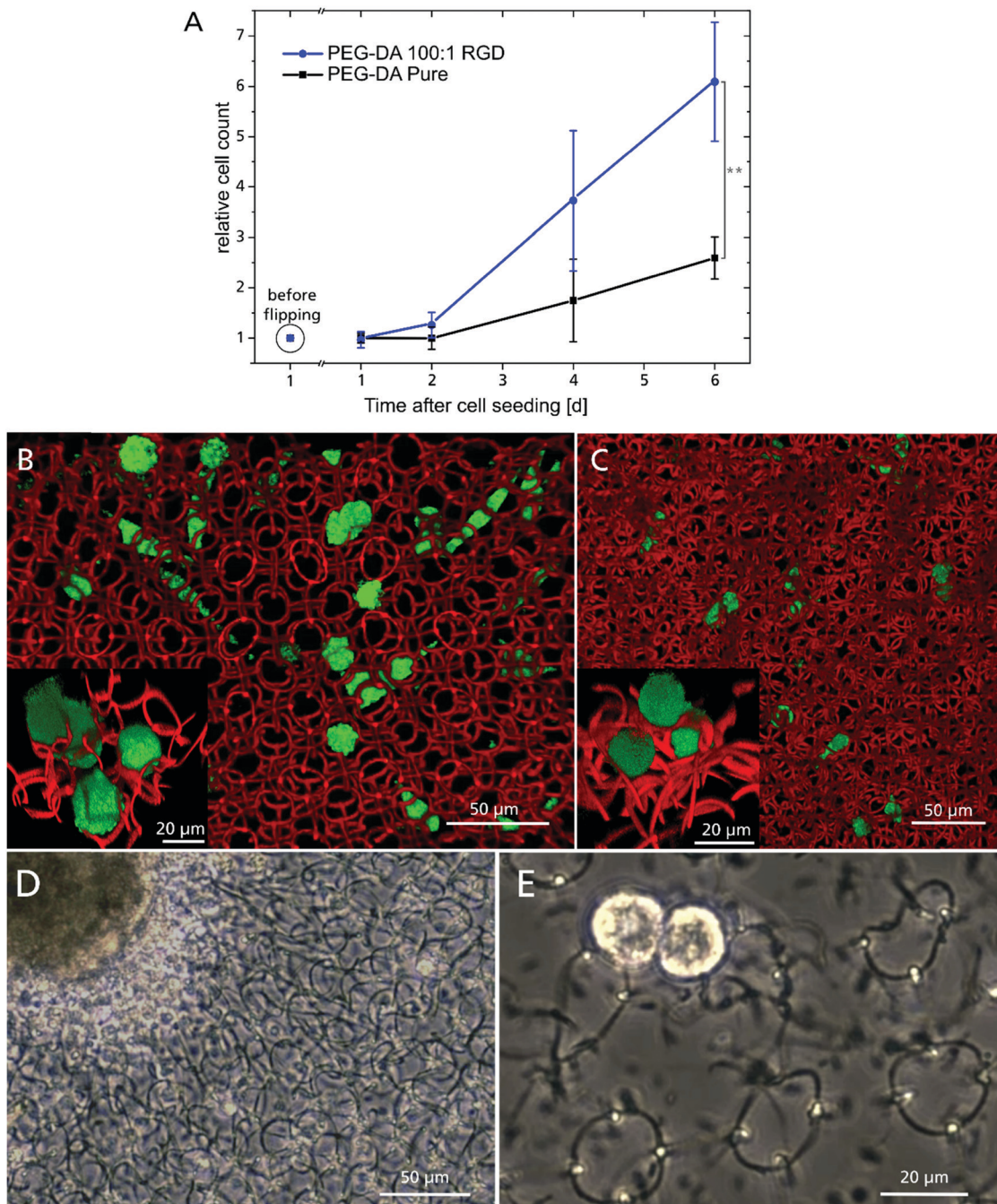


Fig. 4 (A) L929 cell proliferation, cultivated overhead from 24 hours until 6 days after seeding, with cell count reference before substrate flipping (\*\*:  $p \leq 0.01$ ). Top view of fluorescent confocal microscopy images of L929 cells migrating inside 3D hydrogel scaffold in the welded (B) and concatenated ring design (C). The insets show a 3D close-up of cells interacting with the hydrogel rings. (D) iPSC derived cardiomyocyte aggregate, cultured on top of a four layered scaffold made of concatenated rings 7 days after seeding. (E) Two cells from a dissociated cardiomyocyte aggregate on a four layered ring scaffold made of welded rings at day 4 after seeding. Both aggregate and single cells exhibit spontaneous beating behavior (Videos ESI† S9).

the 2PP structured polymer can be varied *via* the laser dosage giving access to Young's moduli between  $(0.46 \pm 0.07)$  MPa and  $(0.09 \pm 0.05)$  MPa.

Inside the highly porous RGD-modified 3D ring-based scaffolds, L929 fibroblast were able to freely migrate in three

dimensions while distorting the delicate hydrogel scaffold, illustrating its flexibility and soft mechanical properties. In preliminary tests, we cultured hiPSC derived cardiomyocytes on these scaffolds for several weeks and observed spontaneous contraction by the cells.

The presented combination of material and 3D fabrication technology has the potential for a major contribution to the biofabrication community, as it offers the possibility of tailoring numerous cell specific parameters such as hydrogel composition, 3D design and (anisotropic) mechanical properties. Our approach is not limited to PEG-DA and should be readily implemented with most photocurable hydrogel precursors allowing adaption of chemical and physical properties and even adjustable biodegradability. By using freeform 3D structuring, it is possible to reduce production time without sacrificing the outstanding resolution of 2PP, possibly accelerating cost-effective production of 2PP generated 3D scaffolds towards large scale manufacturing. As a result, new possibilities for cell culture, lab-on-a-chip devices and tissue engineering applications may become available. In these fields, the monitoring of single cells and the muscle tissue is very important and is being intensively researched.<sup>66,67</sup> Here our method may have the potential to make a contribution in the development of sensory devices.

## Conflicts of interest

The authors have no conflicts to declare.

## Acknowledgements

We like to thank Gerhard Domann and Sönke Steenhusen (Fraunhofer ISC, Optics & Electronics department) for extensive support and fruitful discussion regarding 2PP technology. For nanoindenter measurements and help in analysis thereof we acknowledge Jakob Pyszkowski from Optics11 Life. We also like to thank Joachim Nickel (Department Tissue Engineering and Regenerative Medicine, University Hospital Würzburg) for providing L929 fibroblasts. Doris Heinrich and Sebastian Hasselmann acknowledge funding from the Fraunhofer Attract program “3DNanoCell” and from the Fraunhofer Project Center for Stem Cell Process Engineering. The authors would like to gratefully acknowledge support by the Deutsche Forschungsgemeinschaft (DFG, German Research Foundation)-project number 326998133-TRR225 (subprojects A03).

## References

- 1 G. S. Hussey, J. L. Dziki and S. F. Badylak, *Nat. Rev. Mater.*, 2018, **3**, 159–173.
- 2 A. M. Rosales and K. S. Anseth, *Nat. Rev. Mater.*, 2016, **1**, 1–15.
- 3 A. V. Taubenberger, S. Girardo, N. Träber, E. Fischer-Friedrich, M. Kräter, K. Wagner, T. Kurth, I. Richter, B. Haller, M. Binner, D. Hahn, U. Freudenberg, C. Werner and J. Guck, *Adv. Biosyst.*, 2019, **3**, 1900128.
- 4 Y. Wang, G. Wang, X. Luo, J. Qiu and C. Tang, *Burns: journal of the International Society for Burn Injuries*, 2012, vol. 38, pp. 414–420.
- 5 H. Jeon, M. Lee, S. Yun, D. Kang, K.-H. Park, S. Choi, E. Choi, S. Jin, J.-H. Shim, W.-S. Yun, B.-J. Yoon and J. Park, *Chem. Eng. J.*, 2019, **360**, 519–530.
- 6 K. Shen, H. Kenche, H. Zhao, J. Li and J. Stone, *Biochem. Biophys. Res. Commun.*, 2019, **508**, 302–307.
- 7 M. J. Dalby, M. O. Riehle, H. Johnstone, S. Affrossman and A. S. G. Curtis, *Cell Biol. Int.*, 2004, **28**, 229–236.
- 8 M. Emmert, P. Witzel, M. Rothenburger-Glaubitt and D. Heinrich, *RSC Adv.*, 2017, **7**, 5708–5714.
- 9 M. Gorelashvili, M. Emmert, K. F. Hodeck and D. Heinrich, *New J. Phys.*, 2014, **16**, 75012.
- 10 F. M. Wunner, M.-L. Wille, T. G. Noonan, O. Bas, P. D. Dalton, E. M. De-Juan-Pardo and D. W. Hutmacher, *Adv. Mater.*, 2018, **30**, e1706570.
- 11 A. Lode, M. Meyer, S. Brüggemeier, B. Paul, H. Baltzer, M. Schröpfer, C. Winkelmann, F. Sonntag and M. Gelinsky, *Biofabrication*, 2016, **8**, 15015.
- 12 C. Tse, R. Whiteley, T. Yu, J. Stringer, S. MacNeil, J. W. Haycock and P. J. Smith, *Biofabrication*, 2016, **8**, 15017.
- 13 P. Danilevicius, R. A. Rezende, F. D. A. S. Pereira, A. Selimis, V. Kasyanov, P. Y. Noritomi, J. V. L. da Silva, M. Chatzinkolaidou, M. Farsari and V. Mironov, *Biointerfaces*, 2015, **10**, 21011.
- 14 Z. Wang, C. Wang, C. Li, Y. Qin, L. Zhong, B. Chen, Z. Li, H. Liu, F. Chang and J. Wang, *J. Alloys Compd.*, 2017, **717**, 271–285.
- 15 M. N. Rahaman, D. E. Day, B. S. Bal, Q. Fu, S. B. Jung, L. F. Bonewald and A. P. Tomsia, *Acta Biomater.*, 2011, **7**, 2355–2373.
- 16 T. Jungst, W. Smolan, K. Schacht, T. Scheibel and J. Groll, *Chem. Rev.*, 2016, **116**, 1496–1539.
- 17 C. de Pascalis and S. Etienne-Manneville, *Mol. Biol. Cell*, 2017, **28**, 1833–1846.
- 18 G. Jacquemet, H. Hamidi and J. Ivaska, *Curr. Opin. Cell Biol.*, 2015, **36**, 23–31.
- 19 B. Spagnolo, V. Brunetti, G. Leménager, E. de Luca, L. Sileo, T. Pellegrino, P. Paolo Pompa, M. de Vittorio and F. Pisanello, *Sci. Rep.*, 2015, **5**, 10531.
- 20 L. Jonušauskas, D. Gailevičius, S. Rekštytė, T. Baldacchini, S. Juodkazis and M. Malinauskas, *Mesoscale Laser 3D Printing*, 2018.
- 21 J. Liu, H. Zheng, P. S. P. Poh, H.-G. Machens and A. F. Schilling, *Int. J. Mol. Sci.*, 2015, **16**, 15997–16016.
- 22 N. Huettner, T. R. Dargaville and A. Forget, *Trends Biotechnol.*, 2018, **36**, 372–383.
- 23 M. J. Wilson, S. J. Liliensiek, C. J. Murphy, W. L. Murphy and P. F. Nealey, *Soft Matter*, 2012, **8**, 390–398.
- 24 L. Moroni, T. Boland, J. A. Burdick, C. de Maria, B. Derby, G. Forgacs, J. Groll, Q. Li, J. Malda, V. A. Mironov, C. Mota, M. Nakamura, W. Shu, S. Takeuchi, T. B. F. Woodfield, T. Xu, J. J. Yoo and G. Vozzi, *Trends Biotechnol.*, 2018, **36**, 384–402.
- 25 X. Zhou, Y. Hou and J. Lin, *AIP Adv.*, 2015, **5**, 30701.
- 26 M. H. Olsen, G. M. Hjortø, M. Hansen, Ö. Met, I. M. Svane and N. B. Larsen, *Lab Chip*, 2013, **13**, 4800–4809.
- 27 J.-F. Xing, M.-L. Zheng and X.-M. Duan, *Chem. Soc. Rev.*, 2015, **44**, 5031–5039.
- 28 J. Torgersen, X.-H. Qin, Z. Li, A. Owsianikov, R. Liska and J. Stampfl, *Adv. Funct. Mater.*, 2013, **23**, 4542–4554.



29 J. Rys, S. Steenhusen, C. Schumacher, C. Cronauer and C. Daraio, *Extreme Mech. Lett.*, 2019, **28**, 31–36.

30 P. Kiefer, V. Hahn, M. Nardi, L. Yang, E. Blasco, C. Barner-Kowollik and M. Wegener, *Adv. Opt. Mater.*, 2020, **8**, 2000895.

31 M. Suter, L. Zhang, E. C. Siringil, C. Peters, T. Luehmann, O. Ergeneman, K. E. Peyer, B. J. Nelson and C. Hierold, *Biomed. Microdevices*, 2013, **15**, 997–1003.

32 G. Huang, L. Wang, S. Wang, Y. Han, J. Wu, Q. Zhang, F. Xu and T. J. Lu, *Biofabrication*, 2012, **4**, 42001.

33 L. Yang, A. El-Tamer, U. Hinze, J. Li, Y. Hu, W. Huang, J. Chu and B. N. Chichkov, *Appl. Phys. Lett.*, 2014, **105**, 41110.

34 O. Society, S. D. Gittard, A. Nguyen, K. Obata, A. Koroleva, R. J. Narayan and B. N. Chichkov, *Biomed. Opt. Express*, 2011, **2**, 3167–3178.

35 S. Steenhusen, F. Burmeister, M. Groß, G. Domann, R. Houbertz and S. Nolte, *Thin Solid Films*, 2018, **668**, 74–80.

36 L. Jonušauskas and M. Malinauskas, in *Mesoscale 3D manufacturing: varying focusing conditions for efficient direct laser writing of polymers*, ed. D. L. Andrews, J.-M. Nunzi and A. Ostendorf, SPIE, 2014, p. 912620.

37 M. Thiel, M. S. Rill, G. von Freymann and M. Wegener, *Adv. Mater.*, 2009, **21**, 4680–4682.

38 M. A. Skylar-Scott, S. Gunasekaran and J. A. Lewis, *Proc. Natl. Acad. Sci. U. S. A.*, 2016, **113**, 6137–6142.

39 A. Lee, A. R. Hudson, D. J. Shiawski, J. W. Tashman, T. J. Hinton, S. Yerneni, J. M. Bliley, P. G. Campbell and A. W. Feinberg, *Science*, 2019, **365**, 482–487.

40 R. D. Farahani, K. Chizari and D. Therriault, *Nanoscale*, 2014, **6**, 10470–10485.

41 N. Vanerio, M. Stijnen, B. A. J. M. de Mol and L. M. Kock, *Photobiomodulation, Photomed., Laser Surg.*, 2019, **37**, 383–394.

42 M. M. Lübtow, M. S. Haider, M. Kirsch, S. Klisch and R. Luxenhofer, *Biomacromolecules*, 2019, **20**, 3041–3056.

43 M. S. Haider, M. M. Lübtow, S. Endres, S. Förster, V. J. Flegler, B. Böttcher, V. Aseyev, A.-C. Pöppler and R. Luxenhofer, *ACS Appl. Mater. Interfaces*, 2020, **12**, 24531–24543.

44 T. Lorson, S. Jaksch, M. M. Lübtow, T. Jüngst, J. Groll, T. Lühmann and R. Luxenhofer, *Biomacromolecules*, 2017, **18**, 2161–2171.

45 L. Hahn, M. Maier, P. Stahlhut, M. Beudert, V. Flegler, S. Förster, A. Altmann, F. Töppke, K. Fischer, S. Seiffert, B. Böttcher, T. Lühmann and R. Luxenhofer, *ACS Appl. Mater. Interfaces*, 2020, **12**, 12445–12456.

46 D. Chimene, R. Kaunas and A. K. Gaharwar, *Adv. Mater.*, 2020, **32**, e1902026.

47 E. K. U. Larsen, N. B. Larsen, K. Almdal, E. K. U. Larsen, N. B. Larsen and K. Almdal, *J. Polym. Sci., Part B: Polym. Phys.*, 2016, **54**, 1195–1201.

48 J.-Y. Chen, J. V. Hwang, W.-S. Ao-Ieong, Y.-C. Lin, Y.-K. Hsieh, Y.-L. Cheng and J. Wang, *Polymers*, 2018, **10**, 1263.

49 C. Kern, M. Kadic and M. Wegener, *Phys. Rev. Lett.*, 2017, **118**, 16601.

50 R. W. Cole, T. Jinadasa and C. M. Brown, *Nat. Protoc.*, 2011, **6**, 1929–1941.

51 S.-H. Park, D.-Y. Yang and K.-S. Lee, *Laser Photonics Rev.*, 2009, **3**, 1–11.

52 M. Capurro and F. Barberis, in *Biomaterials for Bone Regeneration//Evaluating the mechanical properties of biomaterials*, ed. M. Capurro and F. Barberis, Elsevier, 2014, pp. 270–323.

53 T.-Y. Huang, M. S. Sakar, A. Mao, A. J. Petruska, F. Qiu, X.-B. Chen, S. Kennedy, D. Mooney and B. J. Nelson, *Adv. Mater.*, 2015, **27**, 6644–6650.

54 A. Marino, J. Barsotti, G. de Vito, C. Filippeschi, B. Mazzolai, V. Piazza, M. Labardi, V. Mattoli and G. Ciofani, *ACS Appl. Mater. Interfaces*, 2015, **7**, 25574–25579.

55 F. Mayer, S. Richter, J. Westhauser, E. Blasco, C. Barner-Kowollik and M. Wegener, *Sci. Adv.*, 2019, **5**, eaau9160.

56 A. C. Lamont, M. A. Restaino, M. J. Kim and R. D. Sochol, *Lab Chip*, 2019, **19**, 2340–2345.

57 J. Torgersen, A. Ovsianikov, V. Mironov, N. Pucher, X. Qin, Z. Li, K. Cicha, T. Machacek, R. Liska, V. Jantsch and J. Stampfl, *J. Biomed. Opt.*, 2012, **17**, 105008.

58 H. K. Heris, J. Daoud, S. Sheibani, H. Vali, M. Tabrizian and L. Mongeau, *Adv. Healthcare Mater.*, 2016, **5**, 255–265.

59 W. Yang, H. Yu, G. Li, Y. Wang and L. Liu, *Biomed. Microdevices*, 2016, **18**, 107.

60 R. Kalluri, *Nat. Rev. Cancer*, 2016, **16**, 582–598.

61 A. E. Miller, P. Hu and T. H. Barker, *Adv. Healthcare Mater.*, 2020, **9**, e1901445.

62 L. Chen, T. Huang, Y. Qiao, F. Jiang, J. Lan, Y. Zhou, C. Yang, S. Yan, K. Luo, L. Su and J. Li, *J. Cell. Biochem.*, 2019, **120**, 8884–8890.

63 J. Wang, J. A. Kaplan, Y. L. Colson and M. W. Grinstaff, *Adv. Drug Delivery Rev.*, 2017, **108**, 68–82.

64 H. Parsa, K. Ronaldson and G. Vunjak-Novakovic, *Adv. Drug Delivery Rev.*, 2016, **96**, 195–202.

65 B. Fischer, A. Meier, A. Dehne, A. Salhotra, T. A. Tran, S. Neumann, K. Schmidt, I. Meiser, J. C. Neubauer, H. Zimmermann and L. Gentile, *Stem Cell Res.*, 2018, **32**, 65–72.

66 Z. Chen, F. Fu, Y. Yu, H. Wang, Y. Shang and Y. Zhao, *Adv. Mater.*, 2019, **31**, e1805431.

67 H. Wang, Y. Liu, Z. Chen, L. Sun and Y. Zhao, *Sci. Adv.*, 2020, **6**, eaay1438.

